Next-generation long-wavelength infrared detector arrays: competing technologies and modeling challenges

Chapter 22

Next-generation long-wavelength infrared detector arrays: competing technologies and modeling challenges

Marco Vallone,[1] Alberto Tibaldi,[1,2] Francesco Bertazzi,[1,2] Andrea Palmieri,[1] Matteo G. C. Alasio,[1] Stefan Hanna,[3] Detlef Eich,[3] Alexander Sieck,[3] Heinrich Figgemeier,[3] Giovanni Ghione[1] and Michele Goano[1,2]

22.1 Introduction

Infrared radiation covers a broad portion of the electromagnetic spectrum spanning a wavelength range from 1.0 μm to 30 μm and beyond, hence between visible light and microwaves. A large part of the infrared spectrum does not reach Earth's ground, because the radiation is blocked by the atmospheric CO_2 and H_2O. The remaining portions of the spectrum are often called "transmission windows" and define the infrared bands that can be used for ground-based infrared imaging systems, see Fig. 22.1: "near-infrared" (NIR, $\lambda = 0.8 \div 1\,\mu$m), "short-wave infrared" (SWIR, $\lambda = 1 \div 3\,\mu$m), "mid-wave infrared" (MWIR, $\lambda = 3 \div 5\,\mu$m), "long-wave infrared" (LWIR, $\lambda = 8 \div 14\,\mu$m), and "very long-wave infrared" (VLWIR, $\lambda = 14 \div 30\,\mu$m, not shown in the figure).

Infrared (IR) imaging is widely used for both military and civilian applications. Military applications include target acquisition, surveillance, night-vision and tracking to guide defense interceptor seekers. Civilian applications include thermography, short-range wireless communication, spectroscopy, weather forecasting and infrared astronomy [1, 2].

An IR detector can sense the energy emitted directly from objects in a scene, which is why they are widely employed for night-vision systems. However, the appearance of an imaged object is mainly determined by its temperature and emissivity. As an object gets hotter, it radiates more energy and appears brighter to a IR imaging system. Instead, emissivity is determined by the imaged object's material. For ex-

[1]Dipartimento di Elettronica e Telecomunicazioni, Politecnico di Torino, Corso Duca degli Abruzzi 24, 10129 Torino, Italy, email michele.goano@polito.it
[2]IEIIT-CNR, Corso Duca degli Abruzzi 24, 10129 Torino, Italy
[3]AIM Infrarot-Module GmbH, Theresienstraße 2, D-74072 Heilbronn, Germany

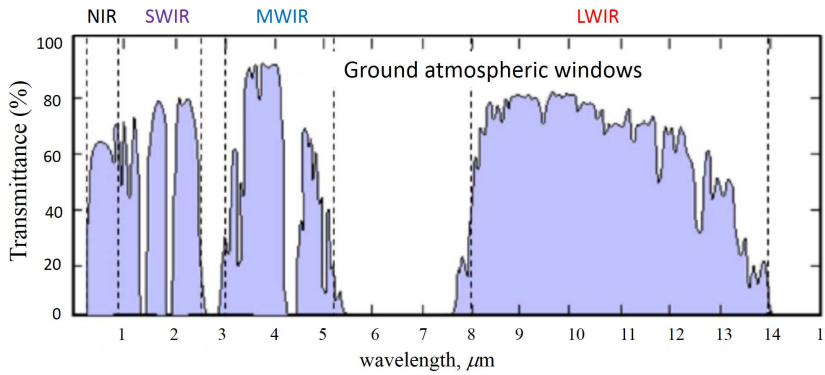

Figure 22.1 Atmospheric transmittance of electromagnetic radiation vs. wavelength (reprinted with permission from [1]).

ample, a cloth has generally lower emissivity than the human skin, which will appear brighter when imaged by a IR FPA detector, even when they have exactly the same temperature.

The choice of the IR sub-bands to by employed in the imaging process depends strongly on the type of atmospheric obscurants interposed between the target and the imager. For example, since smoke particle size ($\approx 0.5\mu$m) is much smaller that typical MWIR or (still better) LWIR wavelength, MWIR and LWIR radiations are less scattered by smoke than NIR or SWIR radiations, which then are better suited to image a scene through smoke. Other applications may require to compare the same scene, when imaged in two or three bands at the same time, in order to detect the temperature of the imaged object. This is of crucial importance in several military applications, in order to identify a possible threat.

Modern IR detection and imaging techniques were first investigated during the Second World War, aiming to obtain true images of the scene in IR bands. First, a simple row of detectors were employed: an image was generated by scanning the scene across the strip using, as a rule, a mechanical scanner (1^{st} generation detectors).

In 1959, Lawson and co-workers [3] triggered the development of variable bandgap $Hg_{1-x}Cd_xTe$ alloys, providing an unprecedented degree of freedom in infrared detector design: in this II-VI pseudo-binary semiconductor alloy, the Γ point direct bandgap can be tuned from that of the semimetal HgTe (-0.3 eV) to that of CdTe (1.5 eV) simply by varying the mole fraction x of the Cd in the composition.

Since the eighties, new photodetectors started to exploit the **photovoltaic effect** in semiconductors (Fig. 22.2). Here, the photons with energy greater than the energy gap, incident on the front surface of the device, generate electron-hole pairs in the material on both sides of the junction. The carriers generated within a diffusion length from the junction reach the space-charge region by diffusion. Then electron-hole pairs are separated by the strong electric field; minority carriers are readily accelerated to become majority carriers on the other side. By this way a photocurrent

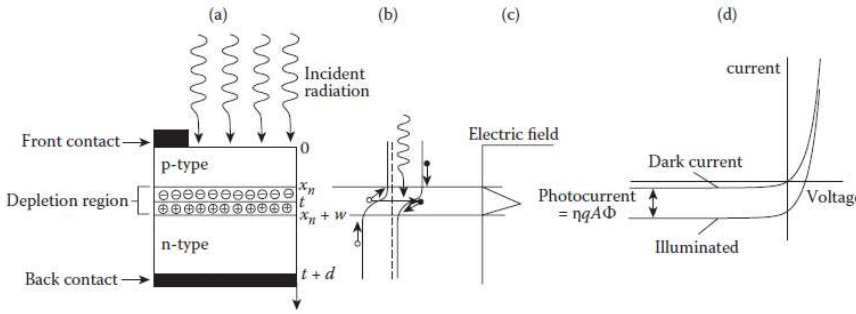

Figure 22.2 *p – n junction photodiode: (a) structure of abrupt junction, (b) energy band diagram, (c) electric field, and (d) current-voltage characteristics for the illuminated and not illuminated photodiode (reprinted with permission from [4, Ch. 9] CRC Press).*

is generated, shifting the current-voltage characteristic in the direction of reverse current (see Fig. 22.2(d)).

Photovoltaic detector arrays are usually illuminated from the back side with photons passing through a transparent detector array substrate, often a CdZnTe layer transparent in IR bands, on which a few microns of HgCdTe (the absorber) are epitaxially grown. The Cd molar fraction of the HgCdTe layer is chosen conveniently, in order to obtain an energy gap suitable for SWIR, MWIR or LWIR bands.

Still during the eighties, new detectors built as two-dimensional (2D) $N \times N$ matrices of pixels – called Focal Plane Arrays (FPAs) – started to be developed (2^{nd} generation detectors, see Fig. 22.3(a-c)), operating in a given wavelength band, normally MWIR or LWIR. At present, most imaging systems can be regarded as composed of an objective with diameter D and focal length F able to image a scene on a focal plane, and a FPA detector like in consumer-grade digital cameras. As a practical concept, each pixel can be regarded as a single detector, capable to convert radiation into an electrical signal.

In the last decades, IR imaging systems evolved to advanced detectors [5] with multicolor capabilities (3^{rd} generation detectors, see Fig. 22.3(d-e)). These systems gather data at the same time in separate IR spectral bands in order to discriminate both absolute temperature and unique signatures of objects in the scene. By providing this new dimension of contrast, multiband detection also enables advanced colour processing algorithms to further improve sensitivity above that of single-colour devices. Such multispectral detection allows for rapid and efficient understanding of the scene in a variety of ways. In particular, two-colour IR FPAs can be especially beneficial for threat-warning military applications. By using two IR wavebands, spurious information, such as background clutter and sun glint, may be subtracted from an IR image, leaving only the objects of interest. Multispectral IR FPAs can also play many important roles in Earth and planetary remote sensing, astronomy, etc.

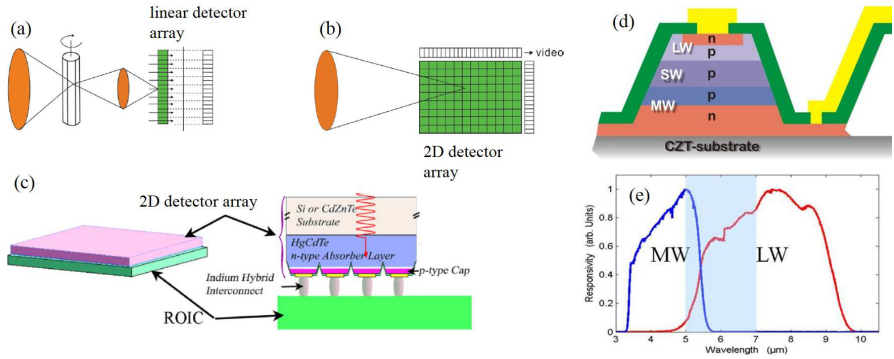

Figure 22.3 *First (a) and second (b) FPAs generation (adapted and reprinted with permission from [6] AIP Publishing). In panel (c), the typical architecture of a HgCdTe-based FPAs with hybridized to a readout integrated circuit (ROIC) (adapted and reprinted with permission from [1]). (d) Schematic of a third-generation dual-band MWIR / LWIR detector pixel; (e) its experimental normalized spectral response spectrum at about 60 K. The cut-off wavelengths of the two bands were 5.4 μm for the MWIR and 9.1 μm for the LWIR band (adapted and reprinted with permission from [7])*

For these reasons, the effective signal-to-noise ratio of two-colour IR FPAs greatly exceeds that of single colour IR FPAs for specific applications.

Most of the radiation emitted in the human environment lies in the MWIR/LWIR bands, which are also known as thermal bands. In this context, optical imaging tools for MWIR and LWIR are commonly referred to as "long-wavelength IR" detection systems. Examples of applications of such instruments include pollution monitoring, gas sensing and spectroscopy based on detecting the chemical species that absorb MWIR and LWIR radiation. Another relevant application involves astronomy, which require very large format, high sensitivity and resolution sensors for both space- or ground-based MWIR and LWIR imaging systems [8,9] (*e.g.*, the wide field IR camera on the Hubble Space Telescope is equipped with a 4096×4096 format charge-coupled-device FPA, with 15 μm-wide pixels [10]). This clarifies why the increasing demand of advanced IR imaging systems for civilian, scientific and military applications has promoted significant efforts towards the development of large format, high sensitivity photodetectors especially for MWIR and LWIR bands (although in the present days SWIR and VLWIR have an increasing importance).

Aiming to minimize the *cost of production*, the most relevant requirements for next-generation IR detectors are

- FPA size
- pixel pitch
- broadband operation
- high operating temperature (HOT) operation

- light coupling capability

In order to avoid over-extending the scope of the chapter and the consequent risk of lessening its usefulness, its focus will be limited a few important points:

- the increasing demand for large FPAs which offer high quality imaging and improved spatial resolution at competitive cost of production
- the necessity to reduce dark current towards the room temperature operability, or at least to achieve detectors with reduced cooling requirements

Even if it will not be described in detail in this chapter, it is worth to mention the possible alternative to HgCdTe-based infrared detection and imaging technology offered by the nearly lattice-matched InAs/GaSb/AlSb material system, also known as the 6.1 Å family [11–14]. The possibility of realizing type-II broken-gap heterostructures and of controlling the energy gap through adjustment of the layer composition and thickness have led to the development of new device concepts and architectures with potentially suppressed Auger generation rates, and consequently lower dark currents and higher operating temperature. Among the proposed architectures [15] are double heterostructures and unipolar-barrier structures such as graded-gap M-, W-structures, nBn, pMp, and pBn detectors, superlattice absorbers surrounded by electron- and hole-blocking unipolar barriers, also known as complementary barrier detectors (CBIRD), pBiBn designs, and interband cascade IR photodetectors (ICIPs) [16].

Besides technological advances in detector material growth and processing, readout circuit design, large FPA hybridization and packaging, further performance improvements of FPAs are possible by integration of photonic functions in FPA detectors (integrated optics). Even if not addressed in this chapter, they include the integration of micro- and nano-structured surfaces (photonic crystals) or photon trapping structures, aimed at increasing the detector quantum efficiency and possibly helpful to reduce the dark current [17, 18] (useful reviews on these arguments can be found in [1, 6, 18, 19]). Optical components based on metasurfaces (arrays of metalenses) have the potential of being monolithically integrated with IR FPAs to increase their operating temperature and sensitivity [20]. In the MWIR, several transparent conducting oxides (TCOs) such as indium tin oxide (ITO) are characterized by a negative real permittivity ($\varepsilon < 0$), allowing to fabricate active plasmonic periodic nanostructures on the illuminated face of FPAs, where the resulting plasmonic resonance wavelength can be tuned by changing the carrier concentration [21].

22.2 Lower cost, large FPAs with subwavelength pixel pitch

Just like for dynamic random access memories (DRAMs) integrated circuits (ICs), the growth rate of the number of pixels on an infrared array (the FPA *size* or *format*) has been growing exponentially for 30 years, in accordance with Moore's Law, with a doubling time of approximately 18 months [18]. As shown in Fig. 22.4(a), astronomical applications may require large format, highly sensitive infrared arrays with size greater than 100 mega pixels. However, the request of large format FPAs is deeply connected with the *pixel pitch*, hence with the number of pixels per

unit area. Before 2000, the typical pixel pitch of IR-FPA detectors ranged between 20 μm and 40 μm without strong incentives towards its reduction, since at that times research was focused on understanding the detector and material physics [22–26], on the development of high quality, low dark current and high sensitivity detectors [4,27–29], on multi-color detector architectures [7,30,31], and on getting larger format FPAs [9, 18]. Recently, cost and performance considerations have driven a significant effort to reduce the pixel pitch, an achievement made possible (see Fig. 22.4(b)) thanks to continuous and substantial technological advancements.

Recent studies indicate as an important technological milestone the development of infrared HgCdTe-based focal plane arrays (FPAs) with sub-wavelength pixel pitch, with the advantage of reducing their volume, lowering their weight and, potentially, cutting their costs. First, when a FPA standard format is selected for production, a smaller pitch corresponds to smaller chips, allowing to fabricate more chips per wafer [32]. Second, under some constraints [33, 34], the reduction of the pixel pitch provides better image quality and improved image resolution, very important features for both military and civilian purposes [6, 9].

The present technologies enabled the production of high quality IR-FPA detectors with pixel size of the order of 10–15 μm [35–37], and high-performance FPAs with pixel dimensions approaching the wavelength scale (Nyquist limit) are under intense investigation [9, 32, 38, 39].

Considering an imaging system composed by a camera objective with focal ratio $F = f/D$ (where f and D are its focal length and aperture diameter, respectively) and a detector, consisting of a FPA with square pixels of pitch d. Its operation ranges between two extremes [9, 32, 38, 39]: the *diffraction-limited* case, if the optical frequency is half the sampling frequency (Nyquist criterion), and the *optics-limited* case, if the Airy disk diameter produced by the lens is equal to d. The two cases are respectively described by the conditions [34]

$$\frac{F\lambda}{d} = \begin{cases} 2 & \text{(diffraction-limited system)} \quad (22.1a) \\ 0.41 & \text{(optics-limited system).} \quad (22.1b) \end{cases}$$

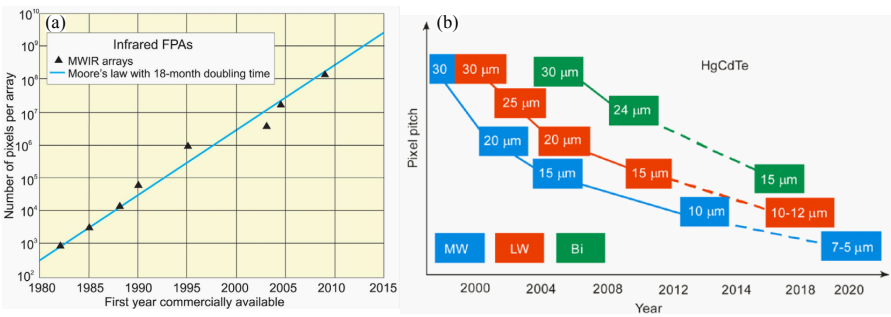

Figure 22.4 (a) The exponential growth, according to Moore's law, of FPAs in last three decades. (b) the continuous decrease of pixel pitch in HgCdTe-based FPAs (adapted and reprinted with permission from [9] IOP Publishing).

If the optical system is limited by diffraction according to the Nyquist criterion (22.1a), further reduction of d is not beneficial in order to maximize the image resolution. On the other hand, when the detector size d equals the diameter of the Airy's disk (optics-limited system), the condition (22.1b) follows, and there is no advantage in increasing d beyond this value.

Equation 22.1a also shows that an optical system with focal ratio $F = 1$ and pixel pitch $d = 5\,\mu$m exhibits performance identical to a more conventional $F = 4$ system with $d = 20\,\mu$m detectors, with the advantage of an overall smaller volume, lower weight and potentially cheaper imaging sensor. Therefore, a diffraction-limited optical system with $F = 1$ and $d = \lambda/2$ appears as an optimal choice [9,38]. However, since detectors operate over a given λ-band and not at a single wavelength, some trade-offs must be accepted, and as reference values, several groups recommend $d = 5 \div 6\,\mu$m for LWIR and $d = 2 \div 3\,\mu$m for MWIR [9,32,38,39].

When such technologically challenging target values for d are considered, it is important to keep under control the inter-pixel crosstalk [17], which includes a number of separate phenomena that may be occurring in the detector or read-out integrated circuit (ROIC) simultaneously. In this Chapter, the following definition is adopted:

> excluding the ROIC, the *inter-pixel crosstalk* can be defined as the electrical response of a FPA pixel when an IR beam illuminates another pixel of the array. Nevertheless, more precise definitions of inter-pixel crosstalk components will be given in Section 22.2.2.

Mesa-type structures [40–43], or microlenses [44, 45] may be helpful to attenuate some of the possible sources of inter-pixel crosstalk. *Diffusive* inter-pixel crosstalk, which is caused by the diffusion of photogenerated carriers in the quasi-neutral region of a pixel [17,34,46], can be prevented, in mesa-type structures, by etching deep trenches between pixels. This is not possible in planar structure, which are widely adopted for large format HgCdTe FPAs. This choice simplifies the technological process (no etching steps), leading to higher quality devices [47]. Nevertheless, planar arrays may be subjected to diffusive inter-pixel crosstalk, that limits the benefits of pitch reduction because of the typically large diffusion length of minority carriers. Indeed, for high quality LWIR detectors, it is of the order of several tens of microns at typical operating temperatures [34].

In order to study and minimize the detrimental effects of inter-pixel crosstalk, realistic, multiphysics, three-dimensional (3D) electromagnetic (optical) and electric simulations are a crucial step for the development of state-of-the-art detectors. Inter-pixel crosstalk can be realistically simulated by illuminating a sub-array (*e.g.*, 5×5) with a Gaussian beam focused on its central pixel, and calculating the photogenerated carrier density G_{opt} by a full-wave electromagnetic simulation based *e.g.* on the finite-difference time-domain (FDTD) method. The outline of the method is reported in Sections 22.2.1 and 22.2.2, along with more precise definitions of inter-pixel crosstalk and an example of calculation.

22.2.1 Comprehensive electromagnetic and electrical simulations

The propagation of electromagnetic waves in any medium is completely described by the solution of Maxwell's equations by means of full-wave numerical schemes. A common practice in FPA detectors is to adopt the FDTD, which is used to discretize and solve Maxwell's equations on a cubic grid known as the Yee grid [48–50].

The absorbed photon density A_{opt} (number of absorbed photons of wavelength λ per unit volume and time) can be evaluated as the divergence of the time-averaged Poynting vector $\langle \vec{S} \rangle$ [45, 51–53]

$$A_{\text{opt}} = -\frac{\vec{\nabla} \cdot \langle \vec{S} \rangle}{h\nu} = \frac{1}{2h\nu}\sigma|\vec{E}|^2, \tag{22.2}$$

where $h\nu$ is the photon energy, $\vec{E}$ its electric field vector, and σ is the electrical conductivity, calculated from the material complex refractive index $\hat{n} = n + i\kappa$ as

$$\begin{aligned} \varepsilon &= n^2 - \kappa^2 = n^2 - \left(\frac{\alpha\lambda}{4\pi}\right)^2 \\ \sigma &= \frac{n\alpha}{\mu_0 c}, \end{aligned} \tag{22.3}$$

where μ_0 is the vacuum magnetic permeability, c is the speed of light in vacuum, and $\alpha = 4\pi\kappa/\lambda$ is the absorption coefficient. The optical generation rate distribution $G_{\text{opt}}(\lambda)$ into the pixel due to interband optical absorption is given by $G_{\text{opt}}(\lambda) = \eta A_{\text{opt}}(\lambda)$, where the quantum yield η, defined as the fraction of absorbed photons which are converted to photogenerated electron-hole pairs, is usually assumed to be unitary.

When the electromagnetic solution is known, the carrier photogeneration rate distribution G_{opt} ensuing from the illumination enters as source term in the continuity equation of a drift-diffusion equations set. The array can be discretized with an appropriate meshing tool which generates a denser grid in regions where gradients of current density, electric field, free charge density and material composition are present. Electric contacts are usually treated as Ohmic with zero resistance, where charge neutrality and equilibrium is assumed, applying ideal Neumann boundary conditions to the outer boundaries of the array. After having appropriately translated the electrical properties of all the FPA array materials (HgCdTe, CdTe, eventual oxide layers, etc.) into the software material library required by the adopted simulation tool, the drift-diffusion equations can be solved by the finite-box method, interpolating on the electric mesh the values of A_{opt} calculated on the Yee's grid. As anticipated, G_{opt} enters the continuity equations for the electron and hole current densities $J_{n,p}$ (where $R_{n,p} - G_{n,p}$ is the net recombination rate in absence of carrier photogeneration)

$$\begin{aligned} \vec{\nabla} \cdot \vec{J_n} &= q(R_n - G_n - G_{\text{opt}}) + q\frac{\partial n}{\partial t} \\ -\vec{\nabla} \cdot \vec{J_p} &= q(R_p - G_p - G_{\text{opt}}) + q\frac{\partial p}{\partial t}, \end{aligned} \tag{22.4}$$

whereas the Poisson equation, to be self-consistently solved with (22.4), current density equations (22.5)

$$\begin{aligned}\vec{J}_n &= qn\mu_n\vec{E} + qD_n\vec{\nabla}n \\ \vec{J}_p &= qp\mu_p\vec{E} - qD_p\vec{\nabla}p,\end{aligned} \tag{22.5}$$

and Fermi distributions, are written as [54, 55]

$$\vec{\nabla}\cdot\varepsilon\left(\vec{\nabla}\psi\right) = -q\left(p - n + N_D^+ - N_A^-\right). \tag{22.6}$$

Here ψ, q, n and p are respectively the electrostatic potential, the elementary charge, electron and hole density, $D_{n,p}$ and $\mu_{n,p}$ are the electron and hole diffusion coefficients and mobilities, and N_D^+ and N_A^- are the ionized donor and acceptor concentrations.

The electrical simulation provides the current under illumination I_i, collected by the i-th pixel's bias contact. If $I_{\text{dark},i}$ is the corresponding dark current, important figures of merit are the photocurrent $I_{ph,i} = I_i - I_{\text{dark},i}$, representing the net contribution to the current resulting from the optical photogeneration, and the i-th pixel quantum efficiency QE_i, defined as

$$\text{QE}_i = \frac{I_{ph,i}}{qN_{\text{phot},i}} \tag{22.7}$$

where $N_{\text{phot},i}$ is the photon flux through its illuminated face, treated as a simulation parameter. If the illuminating beam is monochromatic, repeating the whole (electromagnetic and electric) simulation for an ensemble of N discrete wavelengths λ_n, the obtained $I_{ph,i}$ and QE_i will be spectral quantities.

22.2.2 *Small pixels and inter-pixel crosstalk in planar FPAs*

As an example of calculation, Fig. 22.5(a-c) reports the G_{opt} distribution, simulated by FDTD by illuminating a planar LWIR 5×5 uniform composition HgCdTe pixel sub-array, cooled at 77 K and sketched in Fig. 22.5(d,e), with a *monochromatic* Gaussian beam centered on its central pixel. The geometry, doping profiles and all the details of the computational method are described in Ref. [34]: in short, the pixels have p-on-n polarity and are identified by a $d \times d \times t_{\text{abs}}$ cell, where $t_{\text{abs}} = 2\,\mu$m is the HgCdTe thickness along the vertical growth direction. The array has a 100% fill factor without any trench between pixels, and three cases were examined, considering $d = 3, 5, 10\,\mu$m. The Gaussian beam were obtained by an optical system with $F = 1$ and numerical aperture $NA = 0.447$, focusing the beam on the central pixel.

It is worth stressing that the tail of a beam focused by an optical system unavoidably illuminates also the nearest neighboring (NNs) and corner neighboring (CNs) pixels around the central pixel (CP) of the miniarray (see their definitions in Fig. 22.5(d)). This is one of the components of the inter-pixel crosstalk, the *optical* crosstalk.

Starting from a set of $G_{\text{opt}}(\lambda_n)$ calculated for an ensemble of N discrete λ_n, and following [46], the inter-pixel *optical* crosstalk can be quantified as the ratio between

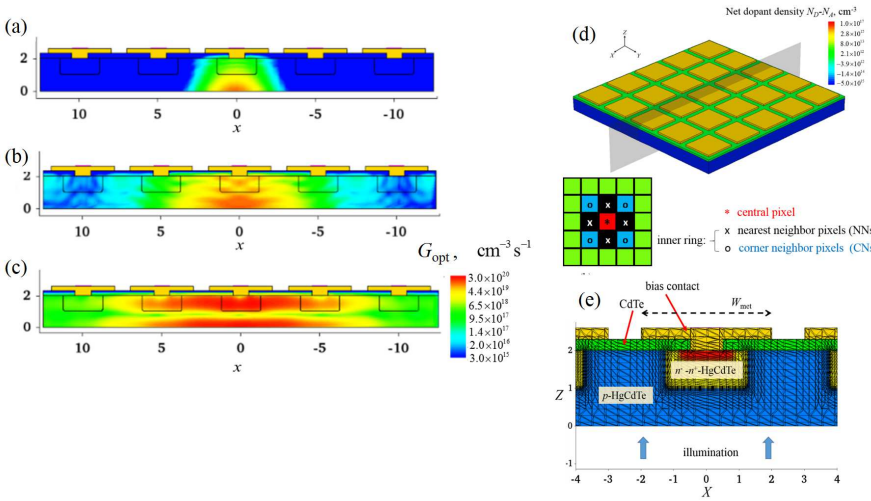

Figure 22.5 *2D distribution of G_{opt}, for a planar LWIR detector with pixel pitch $d = 5\,\mu$m, when illuminated with a monochromatic Gaussian beam ($\lambda = 2, 5, 9.5\,\mu$m (panels (a), (b), and (c), respectively). The detector scheme is sketched in panels (d, e) (adapted and reprinted with permission from [34]).*

carriers photogenerated in the i-th pixel (with volume V_i) and those photogenerated in the whole array (with volume Ω):

$$\mathscr{O}_i = \frac{\int_{V_i} G_{\rm opt}(x,y,z)\,dx\,dy\,dz}{\int_{\Omega} G_{\rm opt}(x,y,z)\,dx\,dy\,dz}. \tag{22.8}$$

It is also important to realize that, even if we illuminate only the central pixel, the photogenerated carriers diffuse in all directions, and a non-negligible photocurrent contribution $I_{ph,i}$ is always present also in each i-th neighboring pixel. In particular, for the considered material, the minority carriers diffusion length $L_{\rm diff}$ is much greater than the pixel pitch ($L_{\rm diff} \approx 150\,\mu$m at 77 K, and the overall lifetime is around $0.3\,\mu$s), so that carrier diffusion is very effective. According to [46], the ratio between the photocurrent in the i-th pixel and the photocurrent in the entire array

$$\mathscr{T}_i = \frac{I_{ph,i}}{\sum_n I_{ph,n}} \tag{22.9}$$

(where the sum is done over all the pixels in the array) may be regarded as the *total* crosstalk, since it depends on both electrical (carrier diffusion related) and optical (beam tail related) effects. Fig. 22.6 reports the simulated spectral QE$_i$ (left column) and crosstalks $\mathscr{O}_i$ and $\mathscr{T}_i$ (right column) for the three considered values of pixel pitch, $d = 3, 5, 10\,\mu$m, for the CP, NNs, and CNs.

Considering the central pixel only, it can be noticed that both $\mathscr{O}_{\rm CP}$ and $\mathscr{T}_{\rm CP}$ (red solid lines and stars) tend to unity for decreasing λ, and increase with d for all wave-

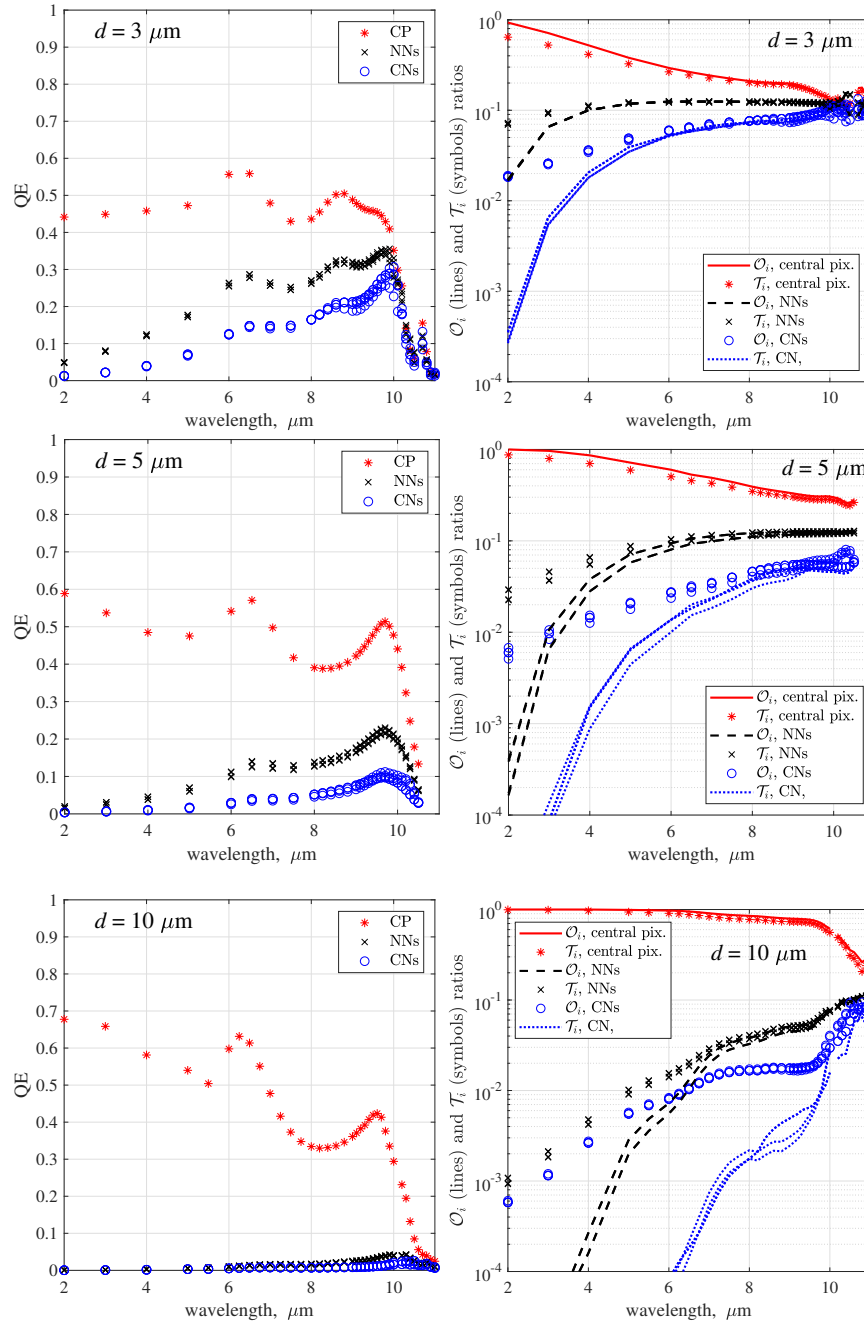

Figure 22.6 *Simulated spectral QE and inter-pixel crosstalk contributions $\mathcal{O}_i$ (lines) and $\mathcal{T}_i$ (symbols), under Gaussian illumination centered on the central pixel, for $d = 3, 5, 10\,\mu$m (adapted and reprinted with permission from [34]).*

lengths, as follows from simple geometrical reasons. Regarding NNs and CNs, both optical and electrical crosstalk concur in determining $\mathscr{T}_i$, although not in a simple additive way, due to the nonlinearity of drift-diffusion equations. The contribution of optical crosstalk becomes progressively less relevant when λ decreases below d, because the beam radius becomes smaller. On the contrary, when $\lambda > d$, the total crosstalk is dominated by the optical contribution ($\mathscr{T}_i \approx \mathscr{O}_i$, both for NNs and CNs). This means that, thanks to the small absorber thickness ($t_{\text{abs}} = 2\,\mu$m), in the spectral interval $\lambda = 5 \div 9\,\mu$m even a pixel pitch as narrow as $3\,\mu$m could allow a total crosstalk $\mathscr{T}_i \approx 0.1$, a value typical of present standard devices [56,57]. Even smaller values of $\mathscr{T}_i$ could be obtained by reducing the electrical crosstalk with non-planar FPAs, like in [1, Ch.7] and [56,58].

In summary, numerical simulation employing Gaussian beam illumination and appropriate definitions for crosstalk can be regarded as a valuable tool for crosstalk investigation.

22.2.3 Modeling photoresponse for non-monochromatic illumination

Generally, the lens of an IR camera focuses a scene containing all the wavelengths in a given spectral window $[\lambda_{\min}, \lambda_{\max}]$, with a spectral power distribution that, at least for thermal sources (*e.g.*, buildings, human bodies, rocket and airplane engines, exhaust gases, etc.), may be well approximated by a Planck's distribution with blackbody temperature T_{B}. Traditional detector arrays are typically designed for narrow band illumination, due to inadequate absorption and charge collection efficiency when photons with very different wavelengths illuminate the FPA. Detector designs overcoming these issues are based on photon-trapping microstructures [17,18,59,60], type-II strained-layer superlattice (SLS) architectures [1,18,61], multispectral adaptive FPAs [6, 62], quantum well IR photodetectors (QWIP) [18], etc. As detectors become increasingly complex, more design variations need to be considered, requesting rapid and efficient simulations without sacrificing the accuracy. For this purpose, it is important to develop modeling methods conceived for efficient simulations of the photoresponse of FPAs illuminated by *non-monochromatic*, *broadband* optical sources.

A possible approach consists in performing a single broadband FDTD optical simulation, using a very narrow time domain Gaussian pulse $\phi(t)$ as input, with spatial Gaussian shape. If we discretize it, a Discrete Fourier Transform (DFT) gives

$$\begin{aligned} \phi(t) &= sin(2\pi\nu_0 t)\,\exp\left(-\frac{t^2}{\tau^2}\right), \quad t = n\Delta t \\ \Phi(\nu_i) &= \sum_{n=0}^{M-1} \phi(n\Delta t)\cos\left(i2\pi\nu_i n\Delta t\right), \end{aligned} \tag{22.10}$$

where M is the number of time steps needed to obtain convergence, ν_0 is the central frequency of the pulse, τ is the temporal pulse width, and Δt is the time step. Typically $\tau \approx \lambda/(2c)$, whereas the choice of Δt depends on the size of the spatial

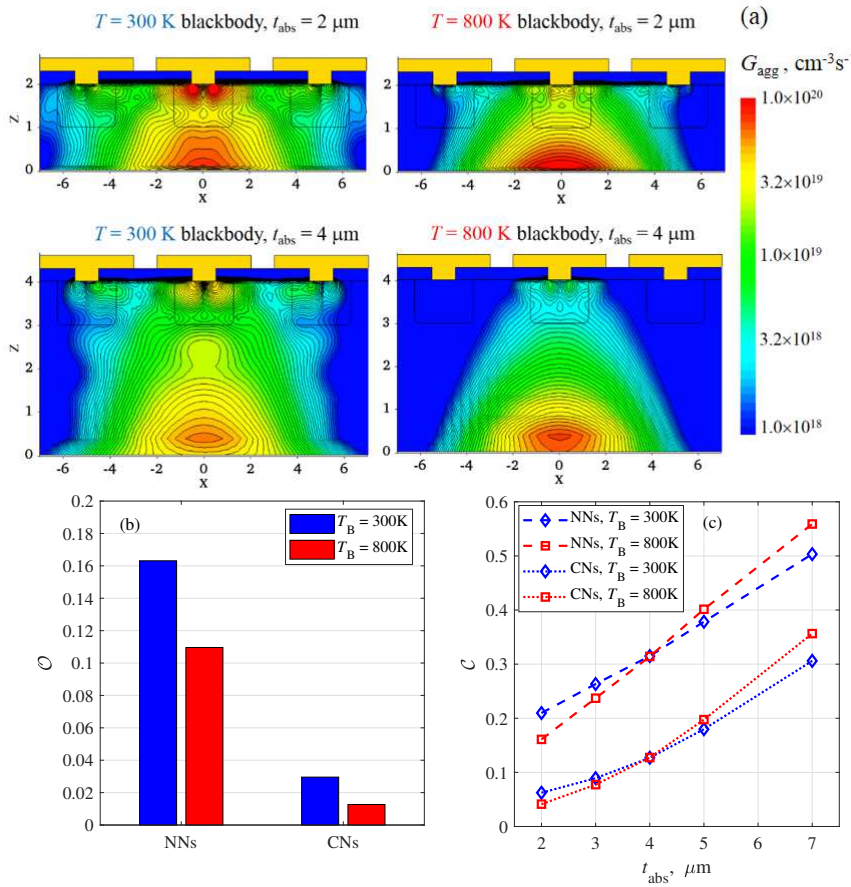

Figure 22.7 *(a) colormaps of G_{agg} distributions obtained with a $T_B = 300\,K$ and $T_B = 800\,K$ blackbody optical source, for $t_{abs} = 2\,\mu m$ (upper row) and $t_{abs} = 4\,\mu m$ (lower row). (b) optical and (c) total inter-pixel crosstalk, for the NNs and CNs (adapted and reprinted with permission from [63]).*

optical mesh, and must fulfill the Courant condition [50, Sec. C.3.2]. For a uniform optical mesh, a spatial step in the order of $\lambda/(10n)$ is often an appropriate choice, and the Courant condition is fulfilled for $\Delta t \approx \lambda/(10nc\sqrt{3})$ or smaller. M depends on the chosen tolerance and therefore is not explicitly set. During the simulation, the $\phi(n\Delta t)$ values are stored and employed to calculate $\Phi(\nu_i)$. If the ϕ's represent the vectors' $\vec{E}$ and $\vec{H}$ components, $\Phi(\nu_i)$ can be used to obtain the rates $A_{i,\mathrm{opt}}$ through the (22.2) at all the frequencies $\{\nu_i\}$ with a single FDTD simulation. The N rates $A_{i,\mathrm{opt}}$ can be then normalized and summed according to the spectral density of the consid-

ered optical source (generally, this should be done by an automatic script integrated in the optical simulator), obtaining the *aggregated* rates A_{agg} and $G_{\mathrm{agg}} = \eta A_{\mathrm{agg}}$ (see Ref. [63] for details on the method).

Following this approach, the effects of the spectral distribution of the IR source (*e.g.*, its blackbody temperature T_{B}, if it is a thermal source), or the effect of detector geometrical parameters can be assessed, employing G_{agg} as the source term of electrical, drift-diffusion based, 3D simulations. Electrical simulations allow to define a useful figure of merit [63], *i.e.* the ratio $\mathscr{C}_i$ between the photocurrent I_{ph} collected by the electrical contact of the i-th pixel and by the miniarray's central pixel CP,

$$\mathscr{C}_i = \frac{I_{ph,i}}{I_{ph,\mathrm{CP}}}, \tag{22.11}$$

that can be regarded as a possible definition of the inter-pixel crosstalk. An example of results can be seen in Fig. 22.7, where the effect of the optical source blackbody temperature T_{B} and the absorber thickness t_{abs} were assessed for the same LWIR detector shown in Fig. 22.5(d,e).

22.3 HOT HgCdTe detectors: technologies and modeling approach

Minimizing the dark current and the noise mechanisms limiting the performance of photodetectors is a fundamental purpose [23]. For these purposes, the first solution is to operate at low temperature, usually around 77 K, in order to reduce the high carrier generation-recombination (GR) rate inherent in all narrow bandgap detectors. However, the required cryogenic cooling of HgCdTe IR detectors is very expensive, and in the last fifteen years huge efforts have been invested to develop detectors with reduced cooling requirements, known as HOT detectors [64–67].

Considering a detector based on a very general photodiode scheme, the dark current depends on intrinsic mechanisms (only related to the material properties), and defect-related mechanisms that depend on bulk and/or surface defects. The first group of mechanisms are

- the Auger and radiative GR in the n- and p-doped regions, generating the ensuing diffusion current,
- the band-to-band tunneling (BTBT),

whereas the most important defect-related mechanisms include

- Shockley-Read-Hall (SRH) GR mechanisms in the depletion region, generating a diffusion current as well
- trap-assisted tunneling
- surface GR processes.

The most important parameter that affects the details of images captured by a FPA is the noise equivalent temperature difference (NETD). This is not strictly related to pixel's geometry and ensuing optical resolution, since it is defined as the temperature difference which would produce a signal equal to the average noise of a

FPA [4,6]. A FPA with good NETD performance is more suitable for detecting slight differences in temperature between objects, which provides more details and more accurate images, with a higher ability to detect smaller objects at greater distances in all weather conditions, an important requirement in many civilian and military applications.

22.3.1 Defects- and tunneling-related dark current

The NETD is heavily affected by the dark current, which is dominated at low temperatures by the diffusion component, while at high temperatures by defect-related components. At increasing operating temperature a growth of the electrically-active defects density occurs, leading to a significant increase of the dark current. Therefore, any approach aiming at reducing one of the dark current components (acting on the related GR-mechanism) is helpful in increasing the maximum temperature at which a FPA can operate.

Reducing or eliminating defect-related GR-mechanisms, the FPA would result Auger-limited, *i.e.*, characterized only by dark-current contributions that can not be eliminated just by an improvement of the material quality (*e.g.*, reducing the impact of SRH mechanism, related to defects density, especially to Hg-vacancies [68]).

Modeling can be very helpful in understanding the contributions of GR-mechanisms to dark current. For example, in Ref. [68] the dark currents of two sets of MWIR detectors with *n*-on-*p* architecture were analyzed. In Fig. 22.8 the 3D structure of a single-pixel, as modeled in [68], is shown. The difference between the two sets was only the adopted doping technique [7, 29]: one set was Hg-vacancy *p*-doped through a standard technology (acceptor concentration $N_A = 2 \times 10^{16}\,\mathrm{cm}^{-3}$), while for the other set Au was used as acceptor ($N_A = 5 \times 10^{15}\,\mathrm{cm}^{-3}$) and the number of Hg vacancies was kept low.

The dark current contributions for these detectors were simulated in the drift-diffusion approximation, and in Fig. 22.9 experimental and simulated dark current densities versus reverse bias are reported. Three-dimensional simulations included

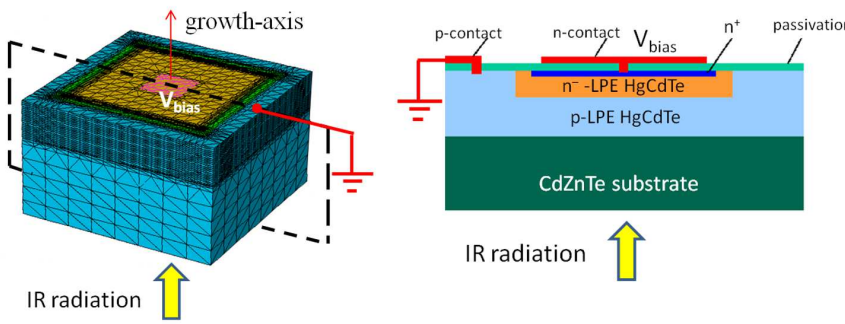

Figure 22.8 3D structure of the MWIR single-pixel photodetectors modeled in [68], with its 2D cross-section at the device center (adapted and reprinted with permission from [68]).

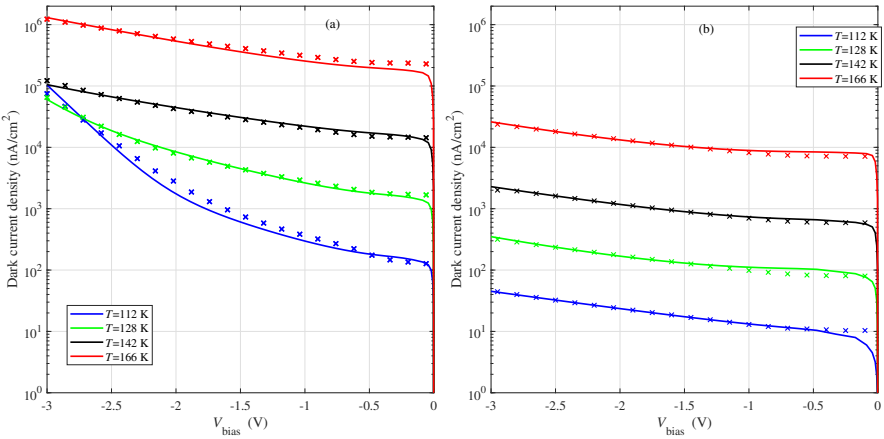

Figure 22.9 Experimental (symbols) and simulated dark current density versus reverse bias V_{bias}, considering the contributions of Auger, SRH, radiative, BTBT and impact ionization GR- mechanisms, for two sets of MWIR FPAs with n-on-p architecture, Hg-vacancy p-doped through a standard technology (a), and Au-doped keeping low the density of vacancies (b) (adapted and reprinted with permission from [68]).

the GR contributions of Auger, SRH, radiative, BTBT and impact ionization GR-mechanisms, for the described two variants of doping.

Regarding BTBT, simulations adopted a less idealized case respect to the classical work by Kane [69], adapting a model proposed in [70, 71], according to which the BTBT generation rate is given by

$$R_{\mathrm{BTBT}} = A\,\delta^{D-1}\mathscr{E}^{\frac{D+1}{2}}\exp\left(-\frac{B}{\delta\sqrt{\mathscr{E}}}\right) \tag{22.12}$$

where $\mathscr{E}$ is the electric field, and the A and B coefficients are [72, 73]

$$A = -\frac{q^2\sqrt{2m_e}}{4\pi^3\hbar^2\sqrt{E_g}}, \quad B = \frac{\pi\sqrt{m_e E_g^3}}{2\sqrt{2}\,q\hbar}. \tag{22.13}$$

The BTBT rate depends on the parameters D (a fitting parameter) and $\delta \approx \sqrt{2qn_iL/\varepsilon}$, where E_g is the bandgap, m_e is the electron's mass, ε is the average dielectric constant, L is the total device length, n_i the intrinsic carrier density, q and $\hbar$ the electron charge and the reduced Planck's constant.

Impact ionization (II) is customarily included in device simulations by means of a semiempirical post-processing involving a bias voltage V dependent gain factor $M(V)$ that multiplies the dark current density $J_{\mathrm{dark}}(V)$ simulated taking into account all other generation mechanisms,

$$J_{\mathrm{dark,II}}(V) = M(V)J_{\mathrm{dark}}(V). \tag{22.14}$$

The advantage of this approximate approach is to avoid the very intensive computations involved by a self-consistent inclusion of II in the DD model, *e.g.*, through the Okuto-Crowell formulation [74]. The gain factor $M(V)$ have the form [75, 76]

$$M(V) = \exp\left[aV \exp\left(-\frac{V_{\text{th}}}{V}\right)\right] \tag{22.15}$$

which depends on the two fitting parameters, a and V_{th}.

Modeling revealed to be very useful *a*) to understand the importance of reducing vacancy density in order to reduce SRH contribution to dark current, and *b*) to ascribe the rapid increase of dark current in Fig. 22.9(a) to the impact ionization, instead of BTBT or trap-assisted-tunneling as initially suspected. An extensive discussion on these points and on the adopted models for BTBT and II can be found in [68].

There are several methods to reduce defects-related contributions to dark current, which can belong to two classes. One approach is based on improving growth and post-growth processing techniques, or to optimize the choice of dopants (*as in the discussed example*), in order to reduce the defect density. The other strategy consists of developing new detector device architectures that are less sensitive to the presence of defects. Some specific approaches are the adoption of high quality passivation, reduction of dislocations, adoption of thin absorber to reduce the material volume when possible, and barrier detectors [77–79].

Among the possible approaches, the unipolar *n*B*n* barrier detectors, whose schematic is shown in Fig. 22.10, is particularly interesting. It consists in a thin wide bandgap layer (represented by the "B") sandwiched between a *n*-doped narrow bandgap absorber (whose thickness should be comparable to the absorption length of light in the device, typically several microns) and a thin *n*-doped narrow bandgap contact region, used to drive the device to reverse bias operation. The important point is to

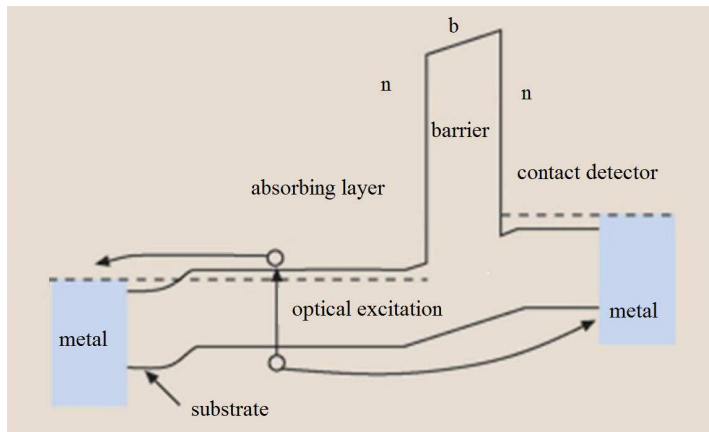

Figure 22.10 Schematic energy band diagram of an ideal nBn detector under (a) zero bias and (b) illumination and low reverse bias V (adapted and reprinted with permission from [6]).

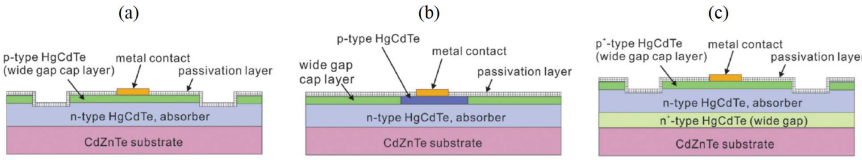

Figure 22.11 Schematic structures for (a) DLHJ, (b) DLPH, and (c) $P^+\nu P^+$ HgCdTe detectors with p-on-n (adapted and reprinted with permission from [6]).

have almost zero valence band offset so that there is no hole barrier present throughout the heterostructure, while a large conduction band offset (electron barrier) is kept. This barrier schematic allows photogenerated minority carrier (holes) to flow to the contact with ease, even at very low bias. Instead, the majority carrier dark current and the (possible) surface current are blocked by the large energy barrier in the conduction band. Since there is no high field depletion region present in the device structure (where SRH GR-processes are very effective), the *n*B*n* detector can effectively suppress and reduce dark current contributions associated with SRH processes and tunneling mechanisms [6].

22.3.2 Auger-suppressed and fully carrier-depleted detectors

In *p*-doped absorbers, the Auger-7 rate is dominant over Auger-1 [23, 80], but its lifetime is much longer than the latter. Therefore, the *n*-on-*p* architecture (a low-*p*-doped absorber sandwiched between a CdTe substrate and a high *n*-doped contact region), which was developed in the early days and used for decades, should be preferable. However, this is not what generally happens.

Detectors based on *n*-on-*p* architectures are fabricated by growing a *p*-type HgCdTe layer using Hg vacancies as acceptors, and obtaining the *np*-junction by ion implantation. In fact, using Hg vacancies in the active layer degrades the minority carriers lifetime, as they increase the SRH GR rate. As a result, the detector exhibits higher dark current than for the case of extrinsic *p*-type doping. Actually, as discussed in Section 22.3.1, possible attempt to reduce the SRH contribution is to avoid Hg vacancies, employing other dopants as acceptors.

Another approach is to adopt *p*-on-*n* architectures, which enable different strategies aimed at reducing the dominant Auger-1 mechanism (that has shorter lifetime than Auger-7) in the *n*-absorber, leading to the so-called Auger-suppressed detectors. This is the approach adopted starting from mid-eighties [6] and now widely implemented.

The reduction of the Auger contribution to dark current can be obtained extending the concept of the *p*-on-*n* architecture to double layer heterojunction (DLHJ), double layer planar heterostructures (DLPH), non-equilibrium $P^+\nu P^+$ or also $P^+N^-n^-N^-N$ architectures [81], see Fig. 22.11. The idea is to exploit low doping levels in the absorber and peculiar band energy profiles to obtain fully carriers depleted absorber at moderate reverse bias voltage. Let us describe this in more detail.

Depleted photodetectors operate under a particular condition: the space charge region should occupy a significant fraction of the detector, *i.e.*, a fraction larger than the quasi-neutral regions. The outcome is a substantial reduction of Auger-1 transitions in the *n*-doped regions, and the ideal situation would be a detector without quasi-neutral regions. In order to understand the trends of carrier generations with doping and band energy profiles, absorber thickness, pixel size, etc., it is not possible to pursue a unique and straightforward modeling approach. For example, the analysis in Ref. [81] were conducted by a combined one-dimensional analytical model, and two-dimensional numerical simulations within the drift-diffusion approximation, each other reciprocally validating their own results.

The approach of carrier depletion may be helpful also in reducing considerably the inter-pixel diffusive crosstalk in dense FPAs, as already argued in quite old works [83, 84]. This issue is particularly complex, and also in this case combined – numerical and analytical – methods of analysis may reveal their strength.

As an example, Ref. [82] investigated the FPA shown and described in Fig. 22.5 by means of three-dimensional numerical simulations, performed by commercial codes that solved the optical problem with the standard full-wave FDTD method and the electrical problem with the finite-box method within the drift-diffusion approximation (see a brief description in Section 22.2.1). The authors calculated the *diffusive inter-pixel crosstalk* that takes place when a realistic, non-monochromatic (blackbody) Gaussian beam is focused on the miniarray's CP, for a few values of absorber

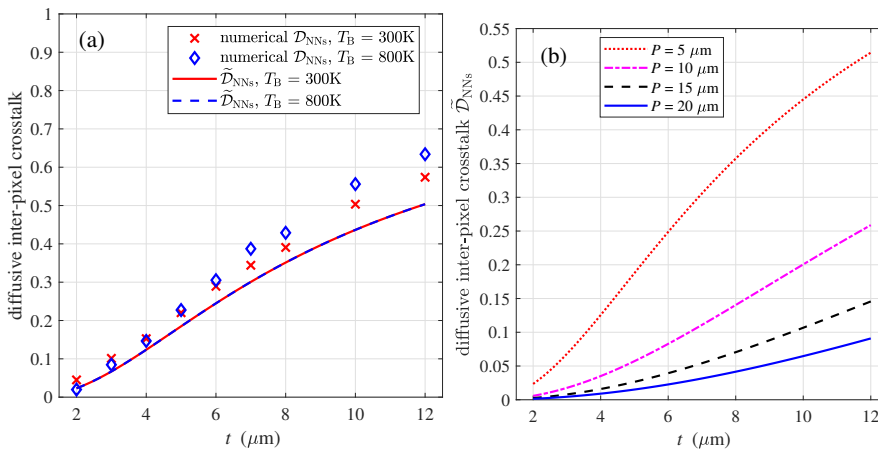

Figure 22.12 *(a) Plot of the diffusive inter-pixel crosstalk $\widetilde{\mathcal{D}}_{NNs}$ according to closed-form model vs. the absorber thickness t, compared with the values of the same crosstalk $\mathcal{D}_{NNs}$ simulated by the numerical model according to the (22.16), for two values of blackbody temperature T_B of the optical source. (b) $\widetilde{\mathcal{D}}_{NNs}(t)$ for several values of pixel pitch P, showing the progressive increase of diffusive inter-pixel crosstalk when P is reduced. Here $T_B = 300\,K$ blackbody illumination is considered (adapted and reprinted with permission from [82]).*

and carrier depletion region thicknesses. The *diffusive* contribution to crosstalk $\mathscr{D}_{\mathrm{NNs}}$ originates from carriers photogenerated in the illuminated pixel that diffuse laterally to the neighboring ones, and it is defined as the ratio

$$\mathscr{D}_{\mathrm{NNs}} = \frac{I_{\mathrm{diff,NNs}}}{I_{ph,\mathrm{CP}}}, \tag{22.16}$$

where $I_{\mathrm{diff,NNs}}$ is the current that carriers, photogenerated in the CP and diffused laterally in neighboring pixels, produce in NNs, and $I_{ph,\mathrm{CP}}$ is the photocurrent collected by the CP.

In parallel an approximate, closed-form model, aimed at better understanding the effects of diffusion on crosstalk was developed. The model avoids to solve the carrier diffusion problem, and it is based instead on a probabilistic description that complements a much more tractable one-dimensional diffusion model. All the details of the closed-form model can be found in [82]. In this way, it was possible to obtain compact expressions for diffusive crosstalk, suitable to develop design rules to keep diffusive crosstalk under control, acting on pixel pitch, absorber thickness, extension and depth of the absorber depleted region. The crucial step was the validation of the closed-form model against the results of three-dimensional numerical simulations for several values of parameters, whose results are shown in Fig. 22.12(a). After this validation step, the model was employed to obtain several trends of $\mathscr{D}_{\mathrm{NNs}}$ with respect to FPA pixel pitch and absorber thickness. An example of the results that can be obtained is reported in Fig. 22.12(b).

22.3.3 Compositionally graded HgCdTe detectors

The approach of carrier-depleting the HgCdTe absorber layer by using appropriate composition and doping profiles [6, 81, 85, 86] has received attention as a method of reducing the dark current, and the adoption of $Hg_{1-x}Cd_xTe$ absorbers with fine-tuned compositional grading is becoming a standard option also in order to optimize the quantum efficiency (QE) and to reduce the inter-pixel crosstalk due to carrier diffusion [87, 88]. For example, Ref. [89] considers a detector, whose scheme is shown in Fig. 22.13, where the absorber layer was given a graded composition, varying the Cd mole fraction from $x = 0.21$ to $x = 0.19$, from its lower to its upper interface, in order to maintain a constant peak wavelength at the temperature of operation. In addition, in order to increase realism, two $0.5\,\mu$m thick transition regions with linear compositional grading connect the low-E_g absorber layer (where E_g is the bandgap) to two high-E_g regions, important to obtain HOT operation. Thus, the capability to numerically predict the performance of FPA infrared detectors with realistic state-of-the-art composition profiles is a present need and an essential step towards their development.

Most commercial 3D device simulators allow to handle the *electrical* modeling of photodetectors, even if compositionally graded. Conversely, the full-wave calculation of G_{opt} may require the development of particular techniques. In fact, the solution of the electromagnetic problem for detectors with arbitrary composition profile may not be straighforward, since not all simulators manage a compositional

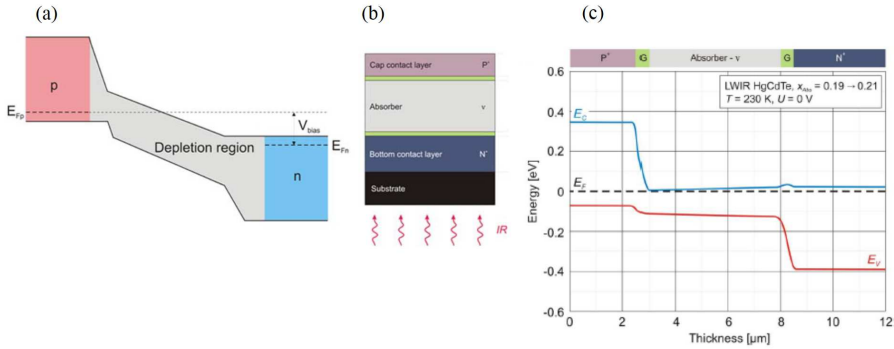

Figure 22.13 *A $p-i-n$ photodiode with compositional grading: (a) reverse bias approximate energy band diagram, (b) its architecture, (c) the calculated energy band diagram at equilibrium (Adapted with permission from [89] C The Optical Society.)*

grading, requiring to define the detector geometry as a stack of layers each with uniform optical properties.

For planar structures, one possible method is to sample the profile, converting it to a staircase, thus discretizing the detector itself into a large stack of layers, each with uniform values for the real and imaginary parts of the HgCdTe refractive index n and κ. Details of the method with hints for its implementation are described in [90]: in short, a Tcl [91] script builds the device geometry, discretizing the compositionally graded layers into N sublayers, building N look-up tables $(\lambda_m, n_m, \kappa_m)_i$, for values $\lambda_m \in [1,20]\,\mu$m, separated by $0.1\,\mu$m. In the end, N material libraries will be produced, allowing the FDTD algorithm to deal with N uniform-composition regions. In Fig. 22.14(a) three-dimensional overall view of a single pixel shows the discretization into $N = 10$ sublayers of the low-E_g absorber region and the two transition regions. In Fig. 22.14(b, c), the real and imaginary parts of the complex refractive index n and κ, calculated for $T = 140$K and $\lambda = 9\mu$m, are shown for a small portion of a vertical two-dimensional (2D) cutplane (the dashed portion shown in panel (a)). In Fig. 22.14(d, e) n and κ are shown along a vertical 1D cutline at center pixel: panel (d) is centered across the low-E_g absorber region, and panel (e) across one of the two transition regions.

The importance of simulating $A_{\text{opt}}(\lambda)$ keeping into account the compositional grading of the detector's absorber depends on the steepness of the grading. If the composition gradient is very low, often an average of composition across the detector is an acceptable approximation. For example, for the structure in Ref. [89], the Cd mole fraction x varies linearly in the absorber in the interval $x \in [0.19, 0.21]$, and the use of an averaged composition is an acceptable approximation. This can be observed in Fig. 22.15(a), where the calculated QE(λ) is shown, comparing FDTD spectra obtained with the described discretization scheme with $N = 10$ (*stars*), or averaging the n and κ in each graded region (*circles*).

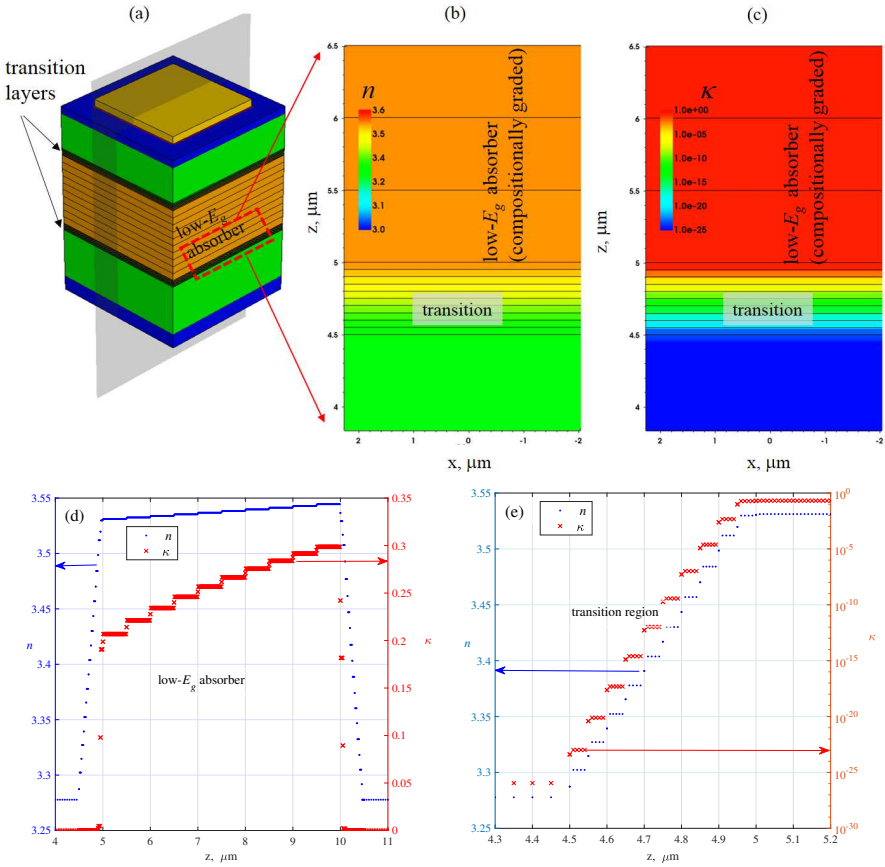

Figure 22.14 (a) 3D overall view of a single pixel, showing the discretization into sublayers of the low-E_g absorber region and the two transition regions. In panels (b) and (c), the real and imaginary parts of the complex refractive index n and κ, calculated for $T = 140K$ and $\lambda = 9\mu m$, are shown for a small portion of a vertical 2D cutplane. In panels (d, e) n and κ are shown along a vertical 1D cutline at center pixel: panel (d) is centered across the low-E_g absorber region, and panel (e) across one of the two transition regions (adapted and reprinted with permission from [90]).

As a counterexample, Fig. 22.15(b) shows the corresponding simulation for a variant of the absorber for which the compositional grading is still linear, but steeper, varying in the interval $x \in [0.19, 0.25]$. It reveals that as soon as moderately steeper profiles are considered, the approximation loses precision, enforcing the necessity of accurate FDTD simulations to obtain reliable modeling results.

Fig. 22.15(a,b) also shows the spectra obtained with the ray tracing, a method based on classical optics and absorption Beer's law [92]. This method is not a valid

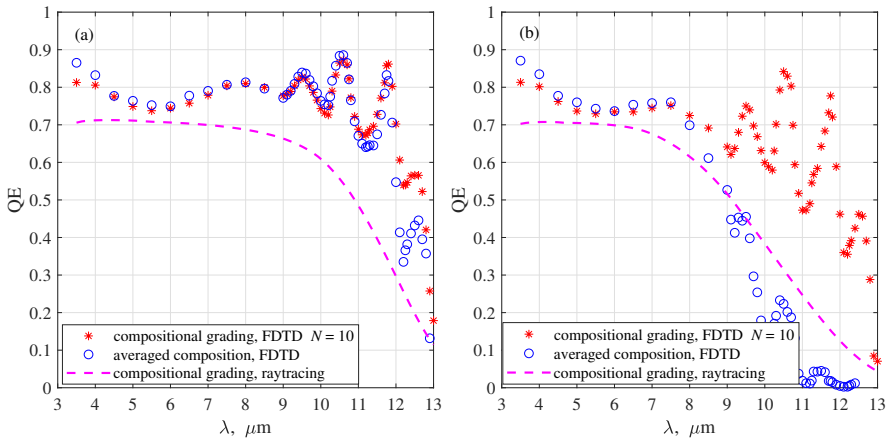

Figure 22.15 *Calculated QE spectra: comparing FDTD spectrum obtained with the described discretization scheme, with* $N = 10$ *(*stars*), or averaging the n and* κ *in each graded region (*circles*). Dashed line, spectrum obtained with the ray tracing method. Panels (a) and (b) refer respectively to the Cd profiles when in the absorber the Cd profile varies linearly in* $x \in [0.19, 0.21]$ *or in the* $x \in [0.19, 0.25]$ *intervals (adapted and reprinted with permission from [90]).*

alternative: since the interfaces with metallizations are highly reflecting in the considered IR bands, large metallization contacts lead to substantial absorption enhancement close to cutoff wavelength, due to spatial resonances and cavity effects [33]. Since ray tracing does not address interference, it often underestimates the cutoff wavelength, as well evident in the cited figures.

Regarding the choice of the discretization parameter N for the FDTD electromagnetic simulation, its value has generally a small impact on the computational cost of the simulation. Consequently, it is recommended to choose a value large enough to sample the absorption coefficient profile $\alpha(z)$ properly, in order to get an accurate estimate of the detector's cutoff wavelength.

22.4 Conclusions

IR FPAs have come a long way since the first photovoltaic two-dimensional arrays were produced in the 1980s. Today they provide nearly ideal background-limited performance that will enable much of the space science over the next decades. The unique properties of HgCdTe, combined with appropriate detector design makes it easy to predict its ongoing leading role in the IR imaging. Nevertheless, Sb-based superlattice fabrication processing is based on standard III-V technology, implying lower costs of mass production and constituting a relatively new alternative for an IR material system in LWIR and VLWIR bands. HOT and fully-depleted (Auger-suppressed) detectors, barrier detectors, multi-bands FPAs, and subwavelength op-

eration are among the key ingredients to obtain IR FPAs with superior performance. In addition, advances in metamaterials and photonic crystal structures let us glimpse new approaches to device design methodologies, improving light coupling with the detector active region and promising several new ways to integrate photonic functions for the enhancement of IR detector performance.

References

[1] Dhar NK, Dat R, Sood AK. Advances in Infrared Detector Array Technology. In: Pyshkin SL, Ballato JM, editors. Optoelectronics. Advanced Materials and Devices. Rijeka, Croatia: IntechOpen; 2013. p. 149–190.

[2] Bhan RK, Dhar V. Recent infrared detector technologies, applications, trends and development of HgCdTe based cooled infrared focal plane arrays and their characterization. Opto-Electron Rev. 2019;27(2):174–193.

[3] Lawson WD, Nielsen S, Putley EH, et al. Preparation and properties of HgTe and mixed crystals of HgTe-CdTe. J Phys Chem Solids. 1959;9(3):325–329.

[4] Rogalski A. Infrared Detectors. 2nd ed. Boca Raton, FL: CRC Press; 2011.

[5] Rogalski A. Infrared Detectors: Status and Trend. Progress Quantum Electron. 2003;27:59–210.

[6] Lei W, Antoszewski J, Faraone L. Progress, challenges, and opportunities for HgCdTe infrared materials and detectors. Appl Phys Rev. 2015;2(4):041303.

[7] Ziegler J, Eich D, Mahlein M, et al. The Development of 3^{rd} Gen IR Detectors at AIM. In: Andresen BF, Fulop GF, Norton PR, editors. Infrared Technology and Applications XXXVII. vol. 8012, Proceedings of the SPIE; 2011. p. 801237.

[8] Gravrand O, Rothman J, Cervera C, et al. HgCdTe detectors for space and science imaging: general issues and latest achievements. J Electron Mater. 2016;45(9):4532–4541.

[9] Rogalski A, Martyniuk P, Kopytko M. Challenges of small-pixel infrared detectors: a review. Rep Prog Phys. 2016;79(4):046501.

[10] Ford HC, Clampin M, Hartig GF, et al. Overview of the Advanced Camera for Surveys on-orbit performance. In: Future EUV/UV and Visible Space Astrophysics Missions and Instrumentation. vol. 4854, Proceedings of the SPIE; 2003. p. 81–94.

[11] Bennett BR, Magno R, Boos JB, et al. Antimonide-based compound semiconductors for electronic devices: A review. Solid-State Electron. 2005;49(12):1875–1895.

[12] Rogalski A, Martyniuk P, Kopytko M. InAs/GaSb type-II superlattice infrared detectors: Future prospect. Appl Phys Rev. 2017;4(3):031304.

[13] Razeghi M, Haddadi A, Dehzangi A, et al. Recent advances in InAs/$InAs_{1-x}Sb_x$/$AlAs_{1-x}Sb_x$ gap-engineered Type-II superlattice-based photodetectors. In: SPIE Defense+Security, Infrared Technology and Applications XLIII. vol. 10177, Proceedings of the SPIE. Anaheim, CA; 2017. p. 1017705.

[14] Klipstein PC, Avnon E, Benny Y, et al. Type II Superlattice Infrared Detector Technology at SCD. J Electron Mater. 2018;47(10):5725–5729.

[15] Sood AK, Zeller JW, Welser RE, et al. Design and development of two-dimensional strained layer superlattice (SLS) detector arrays for IR applications. In: Nayak PK, editor. Two-dimensional materials for photodetector. Rijeka, Croatia: IntechOpen; 2018. p. 103–138.

[16] Tian Z, Hinkey RT, Yang RQ, et al. Interband cascade infrared photodetectors with enhanced electron barriers and *p*-type superlattice absorbers. J Appl Phys. 2012;111(8):024510.

[17] Schuster J, Pinkie B, Tobin S, et al. Numerical Simulation of Third-Generation HgCdTe Detector Pixel Arrays. IEEE J Select Topics Quantum Electron. 2013;19(5):800415.

[18] Martyniuk P, Antoszewski J, Martyniuk M, et al. New concepts in infrared photodetector designs. Appl Phys Rev. 2014;1:041102.

[19] Kinch MA. The Future of Infrared; III-Vs or HgCdTe? J Electron Mater. 2015;44(9):2969–2976.

[20] Zhang S, Soibel A, Keo SA, et al. Solid-immersion metalenses for infrared focal plane arrays. Appl Phys Lett. 2018;113:111104.

[21] Vanamala N, Santiago KC, Das NC. Enhanced MWIR absorption of HgCdTe (MCT) via plasmonic metal oxide nanostructures. AIP Adv. 2019;9:025113.

[22] Kinch MA, Brau MJ, Simmons A. Recombination mechanisms in 8–14–μ HgCdTe. J Appl Phys. 1973;44(4):1649–1663.

[23] Kinch MA. Fundamental physics of infrared detector materials. J Electron Mater. 2000;29(6):809–817.

[24] Kinch MA. Fundamentals of Infrared Detector Materials. Bellingham, WA: SPIE; 2007.

[25] Bertazzi F, Moresco M, Penna M, et al. Full-band Monte Carlo simulation of HgCdTe APDs. J Electron Mater. 2010;39(7):912–917.

[26] Bertazzi F, Goano M, Bellotti E. Calculation of Auger lifetime in HgCdTe. J Electron Mater. 2011;40(8):1663–1667.

[27] Tennant WE, Lee D, Zandian M, et al. MBE HgCdTe technology: A very general solution to IR detection, described by "Rule 07", a very convenient heuristic. J Electron Mater. 2008;37(9):1406–1410.

[28] Kinch MA. HgCdTe: Recent Trends in the Ultimate IR Semiconductor. J Electron Mater. 2010;39(7):1043–1052.

[29] Wollrab R, Schirmacher W, Schallenberg T, et al. Recent progress in the development of hot MWIR detectors. In: 6th International Symposium on Optronics in Defence and Security (OPTRO 2014). Paris; 2014. .

[30] Coussa RA, Gallagher AM, Kosai K, et al. Spectral crosstalk by radiative recombination in sequential-mode, dual mid-wavelength infrared band HgCdTe detectors. J Electron Mater. 2004 Jun;33(6):517–525.

[31] Sood AK, Egerton JE, Puri YR, et al. Design and development of multicolor MWIR/LWIR and LWIR/VLWIR detector arrays. J Electron Mater. 2005 Jun;34(6):909–912.

[32] Holst GC, Driggers RG. Small detectors in infrared system design. Opt Eng. 2012;51(9):096401.

[33] Vallone M, Goano M, Bertazzi F, et al. Comparing FDTD and ray tracing models in the numerical simulation of HgCdTe LWIR photodetectors. J Electron Mater. 2016;45(9):4524–4531.

[34] Vallone M, Goano M, Bertazzi F, et al. Simulation of small-pitch HgCdTe photodetectors. J Electron Mater. 2017;46(9):5458–5470.

[35] Strong RL, Kinch MA, Armstrong JM. Performance of 12-μm- to 15-μm-pitch MWIR and LWIR HgCdTe FPAs at elevated temperatures. J Electron Mater. 2013;42(11):3103–3107.

[36] Reibel Y, Péré-Laperne N, Augey T, et al. Getting small: new 10μm pixel pitch cooled infrared products. In: Infrared Technology and Applications XL. vol. 9070, Proceedings of the SPIE; 2014. p. 907034.

[37] Reibel Y, Péré-Laperne N, Augey LRT, et al. Update on 10 μm pixel pitch MCT-based focal plane array with enhanced functionalities. In: Infrared Technology and Applications XLI. vol. 9451, Proceedings of the SPIE; 2015. p. 945110.

[38] Driggers RG, Vollmerhausen R, Reynolds JP, et al. Infrared detector size: how low should you go? Opt Eng. 2012;51(6):063202.

[39] Tennant WE, Gulbransen DJ, Roll A, et al. Small-pitch HgCdTe photodetectors. J Electron Mater. 2014;43(8):3041–3046.

[40] Nedelcu A, Hamon G, Digonnet A, et al. Low pitch LWIR QWIPs: Performance level and image quality. Infrared Phys Tech. 2014;70(Supplement C):129–133.

[41] McEwen RK, Jeckells D, Bains S, et al. Developments in reduced pixel geometries with MOVPE grown MCT arrays. In: Infrared Techology and Applications XLI. vol. 9451, Proceedings of the SPIE; 2015. p. 94512D.

[42] Rafol SB, Gunapala SD, Ting DZ, et al. Low frequency $1/f$ noise on QWIPs, nBn, and superlattice focal plane array. Infrared Phys Tech. 2017;84:50–57.

[43] Figgemeier H, Hanna S, Eich D, et al. State-of-the-art MCT photodiodes for cutting-edge sensor applications by AIM. In: Infrared Techology and Applications XLIII. vol. 10177, Proceedings of the SPIE; 2017. p. 101771K.

[44] Akın O, Demir HV. Mid-wave infrared metasurface microlensed focal plane array for optical crosstalk suppression. Opt Express. 2015;23(21):27020–27027.

[45] Akın O, Demir HV. High-efficiency low-crosstalk dielectric metasurfaces of mid-wave infrared focal plane arrays. Appl Phys Lett. 2017;110:143106.

[46] Pinkie B, Bellotti E. Numerical simulation of spatial and spectral crosstalk in two-color MWIR/LWIR HgCdTe infrared detector arrays. J Electron Mater. 2013;42(11):3080–3089.

[47] Hanna S, Eich D, Mahlein KM, et al. MCT-based LWIR and VLWIR 2D focal plane detector arrays for low dark current applications at AIM. J Electron Mater. 2016;45(9):4542–4551.

[48] Yee K. Numerical solution of initial boundary value problems involving Maxwell's equations in isotropic media. IEEE Trans Antennas Propagation. 1966 May;14(3):302–307.

[49] Berenger JP. A perfectly matched layer for the absorption of electromagnetic waves. J Comp Phys. 1994;114(2):185–200.

[50] Vasileska D, Goodnick SM, Klimeck G. Computational Electronics. Semiclassical and Quantum Device Modeling and Simulation. Boca Raton, FL: CRC Press; 2010.

[51] Born M, Wolf E. Principles of Optics. Electromagnetic Theory of Propagation, Interference and Diffraction of Light. 7th ed. Cambridge, U.K.: Cambridge University Press; 1999.

[52] Keasler C, Bellotti E. Three-dimensional electromagnetic and electrical simulation of HgCdTe pixel arrays. J Electron Mater. 2011;40(8):1795–1801.

[53] Liang J, Hu W, Ye Z, et al. Improved performance of HgCdTe infrared detector focal plane arrays by modulating light field based on photonic crystal structure. J Appl Phys. 2014;115(18):184504.

[54] Sze SM. Physics of Semiconductor Devices. 2nd ed. New York: John Wiley & Sons; 1981.

[55] Selberherr S. Analysis and Simulation of Semiconductor Devices. Wien: Springer-Verlag; 1984.

[56] Wehner JGA, Smith EPG, Radford W, et al. Crosstalk modeling of small-pitch two-color HgCdTe photodetectors. J Electron Mater. 2012;41(10):2925–2927.

[57] Armstrong JM, Skokan MR, Kinch MA, et al. HDVIP five-micron pitch HgCdTe focal plane arrays. In: Infrared Technology and Applications XL. vol. 9070, Proceedings of the SPIE; 2014. p. 907033.

[58] Knowles P, Hipwood L, Shorrocks N, et al. Status of IR detectors for high operating temperature produced by MOVPE growth of MCT on GaAs substrates. In: Electro-Optical and Infrared Systems: Technology and Applications IX. vol. 8541, Proceedings of the SPIE; 2012. p. 854108.

[59] Wehner JGA, Smith EPG, Venzor GM, et al. HgCdTe photon trapping structure for broadband mid-wavelength infrared absorption. J Electron Mater. 2011;40(8):1840–1846.

[60] Schuster J, Bellotti E. Analysis of optical and electrical crosstalk in small pitch photon trapping HgCdTe pixel arrays. Appl Phys Lett. 2012;101(26):261118.

[61] Rogalski A, Martyniuk P, Kopytko M. Type-II superlattice photodetectors versus HgCdTe photodiodes. Progress Quantum Electron. 2019;p. 100228.

[62] Rogalski A, Antoszewski J, Faraone L. Third-generation infrared photodetector arrays. J Appl Phys. 2009;105(9):091101.

[63] Vallone M, Palmieri A, Calciati M, et al. Non-monochromatic 3D optical simulation of HgCdTe focal plane arrays. J Electron Mater. 2018;47(10):5742–5751.

[64] Ashley T, Elliott CT. Model for minority carrier lifetimes in doped HgCdTe. Electron Lett. 1985;21(10):451–452.

[65] Elliott CT. Non-equilibrium modes of operation of narrow-gap semiconductor devices. Semiconductor Sci Tech. 1990;5(35):S30.

[66] Martyniuk P, Rogalski A. HOT infrared photodetectors. Opto-Electron Rev. 2013;21(2):239–257.

[67] Wang P, Xia H, Li Q, et al. Sensing infrared photons at room temperature: from bulk materials to atomic layers. SMALL. 2019;15(46):1904396.

[68] Vallone M, Mandurrino M, Goano M, et al. Numerical Modeling of SRH and Tunneling Mechanisms in High-Operating-Temperature MWIR HgCdTe Photodetectors. J Electron Mater. 2015;44(9):3056–3063.

[69] Kane EO. Theory of tunneling. J Appl Phys. 1961;32(1):83–89.

[70] Verhulst AS, Leonelli D, Rooyackers R, et al. Drain voltage dependent analytical model of tunnel field-effect transistors. J Appl Phys. 2011;110(2):024510.

[71] Ahmed K, Elahi MMM, Islam MS. A compact analytical model of band-to-band tunneling in a nanoscale p-i-n diode. In: 2012 International Conference on Informatics, Electronics and Vision (ICIEV); 2012. .

[72] Adar R. Spatial integration of direct band-to-band tunneling currents in general device structures. IEEE Trans Electron Devices. 1992 Appl Phys Rev;39(4):976–981.

[73] Jóźwikowski K, Kopytko M, Rogalski A, et al. Enhanced numerical analysis of current-voltage characteristics of long wavelength infrared *n*-on-*p* HgCdTe photodiodes. J Appl Phys. 2010;108(7):074519.

[74] Okuto Y, Crowell CR. Energy-conservation considerations in the characterization of impact ionization in semiconductors. Phys Rev B. 1972 Oct;6(8):3076–3081.

[75] Elliott CT, Gordon NT, Hall RS, et al. Reverse breakdown in long wavelength lateral collection $Cd_xHg_{1-x}Te$ diodes. J Vac Sci Technol A. 1990;8(2):1251–1253.

[76] Rothman J, Mollard L, Goût S, et al. History-dependent impact ionization theory applied to HgCdTe e-APDs. J Electron Mater. 2011;40(8):1757–1768.

[77] Maimon S, Wicks GW. *nBn* detector, an infrared detector with reduced dark current and higher operating temperature. Appl Phys Lett. 2006;89(15):151109.

[78] Itsuno AM, Phillips JD, Velicu S. Predicted performance improvement of Auger-suppressed HgCdTe photodiodes and *p*-*n* heterojunction detectors. IEEE Trans Electron Devices. 2011 Feb;58(2):501—507.

[79] Itsuno AM, Phillips JD, Velicu S. Mid-wave infrared HgCdTe nBn photodetector. Appl Phys Lett. 2012 Appl Phys Rev;100(16):161102.

[80] Kinch MA, Aqariden F, Chandra D, et al. Minority Carrier Lifetime in *p*-HgCdTe. J Electron Mater. 2005;34(6):880–884.

[81] Schuster J, Tennant WE, Bellotti E, et al. Analysis of the Auger recombination rate in $P^+N^-n^-N^-N$ HgCdTe detectors for HOT applications. In: Infrared Technology and Applications XLII. vol. 9819, Proceedings of the SPIE; 2016. p. 98191F.

[82] Vallone M, Goano M, Bertazzi F, et al. Diffusive-probabilistic model for inter-pixel crosstalk in HgCdTe focal plane arrays. IEEE J Electron Devices Soc. 2018;6(1):664–673.

[83] Kamins TI, Fong GT. Photosensing Arrays with Improved Spatial Resolution. IEEE Trans Electron Devices. 1978;25(2):154–159.

[84] Dhar V, Bhan RK, Ashokan R. Effect of built-in electric field on crosstalk in focal plane arrays using HgCdTe epilayers. Infrared Phys Tech. 1998;39(6):353–367.

[85] Martyniuk P, Gawron W, Pawluczyk J, et al. Dark current suppression in HOT LWIR HgCdTe heterostructures operating in non-equilibrium mode. J Infrared Millim Waves. 2015;34:385–390.

[86] Schuster J, DeWames RE, Wijewarnasurya PS. Dark currents in a fully-depleted LWIR HgCdTe *P*-on-*n* heterojunction: analytical and numerical simulations. J Electron Mater. 2017;46(11):6295–6305.

[87] Vallone M, Goano M, Bertazzi F, et al. Reducing inter-pixel crosstalk in HgCdTe detectors. Opt Quantum Electron. 2020;52(1):25.

[88] Vallone M, Goano M, Bertazzi F, et al. Constraints and performance tradeoffs in Auger-suppressed HgCdTe focal plane arrays. Appl Opt. 2020;59(?):??

[89] Rogalski A, Kopytko M, Martyniuk P. Performance prediction of p-i-n HgCdTe long-wavelength infrared HOT photodiodes. Appl Opt. 2018;57(18):D11–D18.

[90] Vallone M, Goano M, Bertazzi F, et al. FDTD simulation of compositionally graded HgCdTe photodetectors. Infrared Phys Tech. 2019;97:203–209.

[91] Ousterhout J, Jones K. Tcl and Tk toolkit. Addison-Wesley Professional; 2010.

[92] Spencer GH, Murty MVRK. General ray-tracing procedure. J Opt Soc Amer. 1962 Jun;52(6):672–676.